Clay/phosphate-based ceramic materials for high temperature thermal energy storage – Part II: Validation of high temperature storage performance at pilot scale

Abdoul Razac Sane, Nawal Semlal, Rachid Boulif, Claudia Toussaint, Alain Germeau, Ange Nzihou, Doan Pham Minh

Solar Energy 278 (2024) 112799

Contents lists available at ScienceDirect

Solar Energy

journal homepage: www.elsevier.com/locate/solener

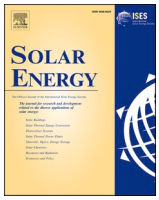

Clay/phosphate-based ceramic materials for high temperature thermal energy storage – Part II: Validation of high temperature storage performance at pilot scale

Abdoul Razac Sane [a,*], Nawal Semlal [b], Rachid Boulif [b], Claudia Toussaint [c], Alain Germeau [c], Ange Nzihou [a], Doan Pham Minh [a,*]

[a] Université de Toulouse, IMT Mines Albi, CNRS, Centre RAPSODEE, Campus Jarlard, F-81013, Albi Cedex 09, France
[b] Innovation, OCP SA, BP 118, 24000 El Jadida, Morocco
[c] PRAYON S.A., rue J. Wauters, 144, B-4480 Engis, Belgium

ARTICLE INFO

Keywords:
Thermal Energy Storage
Phosphate
Clay
Thermocline
Pilot scale
Industrial decarbonization

ABSTRACT

The performances of a pilot scale packed bed thermal energy storage system filled with 162 kg of developed phosphate-based ceramic materials (cylinders of 1.5 cm × 4 cm) was experimentally investigated under different operating conditions of inlet air temperature for the charge (334 +/- 21 °C, 531 +/- 23 °C and 760 +/- 15 °C), air flowrate for charging and discharging (26.5 to 74 kg/h), as well as under consecutive cycles.

The packed bed performed well at different temperature and charge / discharge flowrate. The cylindrical shape of the produced clay/phosphate-based ceramic combined with the horizontal implementation of the storage tank did not provoke a significant preferential path for the air inside the storage medium and did not create a significant thermal de-stratification during the charging and discharging phases. Furthermore, under consecutive cycles, the TES system could be quickly stabilized demonstrating the robustness and flexibility of the developed TES system, which can cover a wide range of application cases. The production of the developed ceramics is mastered by ceramic industries allowing the availability at industrial scale worldwide with competitive cost and carbon footprint.

This work opens new prospects for using phosphates-based ceramics as alternative promising media to build new generation of flexible and reliable high temperature TES system for industrial assets decarbonation, grid services as well as renewable energies high penetration into the grid.

1. Introduction

To mitigate global climate change and the associated negative consequences on natural and human systems, it is necessary to reduce the GHG emissions as fast as possible. Integrating renewable energy systems in substitution to fossil fuel is indispensable for achieving the energy transition target. But the availability of renewable sources such as solar and wind is intermittent at daily and seasonal scale, and is dependent on the weather conditions. Energy storage is mandatory to regulate the dephasing of energy availability and demand [1,2]. Electricity production by photovoltaic (PV) has been largely industrialized but storing electricity by an efficient and economical manner is still a great challenge. As an alternative solution, the energy collected from PV, Wind Turbine Generators (WTG) or Concentrated Solar Technologies (CST) can be stored in the form of heat in a long duration Thermal Energy Storage system (TES). In such a system, hybrid or not, heat can be stored when the resource is abundant and later restored under the form of electricity and/or heat, which can contribute to shape the energy supply and demand. To-date, conventional Concentrated Solar Power plants (CSP) can produce electricity from solar energy, with possibility of TES integration, which can ensure a 24/24 electricity production without any use of fossil fuel [3,4 5 6 7]. However, the cost of the commercial product (electricity) is still high (>0.20 $/kWh), causing the limited expansion of this technology [1]. Improving the storage system, particularly to reach high temperature thermal energy storage offers a promising way to increase the global efficiency of CSP plants, thus, contributing to the reduction cost of the final product.

Currently, the most developed TES concept for industrial scale use two tanks molten salt systems, allowing typically heat storage for 6–18

* Corresponding authors.
E-mail addresses: asane@mines-albi.fr (A. Razac Sane), doan.phamminh@mines-albi.fr (D. Pham Minh).

https://doi.org/10.1016/j.solener.2024.112799
Received 30 January 2024; Received in revised form 20 June 2024; Accepted 19 July 2024
Available online 25 July 2024

Nomenclature

Greek letters

β	Threshold coefficient (%)
ε	Porosity (%)
η	Charging or discharging rate (%)
λ	Thermal conductivity (W/m/K)
Ø	Dimensionless axial air temperature distribution calculated by T/Tmax, where T is the measured air temperature at a certain time and Tmax the hot inlet air temperature

Latin letters

$\dot{m}$	Mass flow rate (kg/h)
Cp	Specific heat (J/kg/K)
E	Energy (kWh)
$Eff_{overall}$	Global efficiency of a given storage cycle (%)
H_{tc}	Thermocline thickness (m)
$H_{tc,max}$	Maximal thermocline thickness (m)
m	Total mass of phosphate-based ceramics (kg)
n	number of storage volume
P_{th}	Recovered thermal power (kW)
$P_{th,max}$	Maximal recovered thermal power (kW)
T	Temperature (°C)
t	Time (h)
x	Axial coordinate of bed (m)

Subscripts

Air	Air
b	Low temperature, beginning of storage charge
ceram	Phosphate-based ceramics
ch	Charge
CSP	Concentrated Solar Power
dis	Discharge
H	High-temperature, end of storage
in	Inlet
max	Maximum
out	Outlet
overall	Overall performance of storage
thr	Threshold

h. Several implantations are operating worldwide such as Andasol [7 8 9 10] in operation since 2008, Gemasolar [11], NOOR I, II & III [12], or more recently the biggest thermal solar project under commissioning in Dubai, DEWA NOOR Energy 1 [13]. In such CSP plants, the storage media consists of molten nitrate salt (commercially named Solar salt@, a mixture of 60 wt% $NaNO_3$ and 40 wt% $KaNO_3$), which is used under the liquid form between 290 and 565 °C [14 15 16]. The two-tank storage concept is chosen for industrial scale because it is effective and easy to handle [17]. However, this configuration presents a relative high capital cost, up to *ca.* 20 % of the total cost of a CSP plant [18 19], and in reality, only one equivalent tank is fully charged at a given time. In addition, the working temperature of molten salt is limited below 565 °C because of the risk of irreversible thermal decomposition, preventing its utilization in systems such as central receiver solar power plants which can reach 800 – 1000 °C [20].

To reduce the cost and boost the performance of the overall power plant, simple TES system concept based on a single tank named "thermocline TES system" has received significant research attention during the last decade [21 22 23 24 25 26 27 28 29 30]. According to Pacheco et al. [31], the thermocline configuration is expected to be 66 % cheaper than conventional two tanks TES using molten salt. In a thermocline TES, a high temperature HTF passes through a storage packed bed for exchanging heat during charging and discharging steps. Cheap and available monolithic materials are generally investigated as storage media and different geometries of storage vessel, including vertical, horizontal, cylindrical, parallelepiped shapes, have been considered to analyze the thermocline performances [54–59].

Depending on the filler material, the thermocline TES system can advantageously use air as HTF and operate at high temperature ranges (>1000 °C) such as in a high temperature central receiver CSP towers [32 33]. Air has been studied by several works and considered as a suitable working fluid considering the following characteristics: free and abundant, no limitation on temperature, does not suffer degradation, no toxicity, no chemical issues, good compatibility with most of storage materials and can operate at high temperature ranges and thus increases the energetic storage capacity.

The single tank thermocline concept, in addition to being able to store heat generated by CSP, is a relevant technology for industrial waste heat recovery, which represent an important source of energy to valorize. According to the French Agency of Energy (ADEME), the industrial waste heat can represent up to 60 % of inlet process energy in heavy industries and is mainly available at high temperature up to 1000 °C [34]. The same observation was commented by the US Department of Energy; they have evaluated these waste heat as around 20 % of the input energy of steelmaking processes and above 25 % for the glass and foundry industries [35]. Furthermore, since the last years, several technologies based on the thermocline concept are in demonstration phase (TRL 4 – 6) in industry worldwide for decarbonization purposes [36]. Various filler materials have been investigated such as volcanic rocks [37 38], alumina [39], concrete [40 41], silica sand [42], graphite blocks [43], graphite-aluminum alloys, ceramics [44], steel [45], industrial by-products based ceramics [51–53]. It is commonly observed that most of high temperature (>650 °C) thermocline TES pilots usually use packed bed of alumina, graphite and rocks beads as TES medium [39 29 36]. Due to the wide variety of rocks (mineral composition, size, geometry) associated to the high degradation; the high cost and high environmental impact of alumina, it is primordial to develop alternative materials, satisfying the main criteria required for a TES material, such as high working temperature range, good availability at the industrial scale, easy processing, low cost, low environmental impact, high thermophysical & thermomechanical properties, and high thermal stability [46 47].

We have recently reported the first research work on clay/phosphate-based ceramic materials for high temperature thermal energy storage [48]. These ceramics were found to be thermally stable at high temperature (>1000 °C) and to have competitive thermo-physical and thermo-mechanical properties. In addition, they are available at large industrial scale worldwide, low carbon footprint, easy to process and are expected to be less expensive than commercially available alumina.

In the present work, these new promising materials are investigated in high temperature TES (up to 800 °C) at the pilot scale, using air as HTF. The objective is to validate the effectiveness and reliability of the thermocline system during a typical operation of the system (full charge and discharge phases). The impact of degraded operational parameters as inlet air mass flow rate and temperature during the two phases of charge and discharge is investigated. Cyclic performance is also studied.

2. Materials and methods

2.1. Ceramics processing

The ceramics used in this study were elaborated by the extrusion of a mixture of clay, a synthetic phosphate (commercial hydroxyapatite from

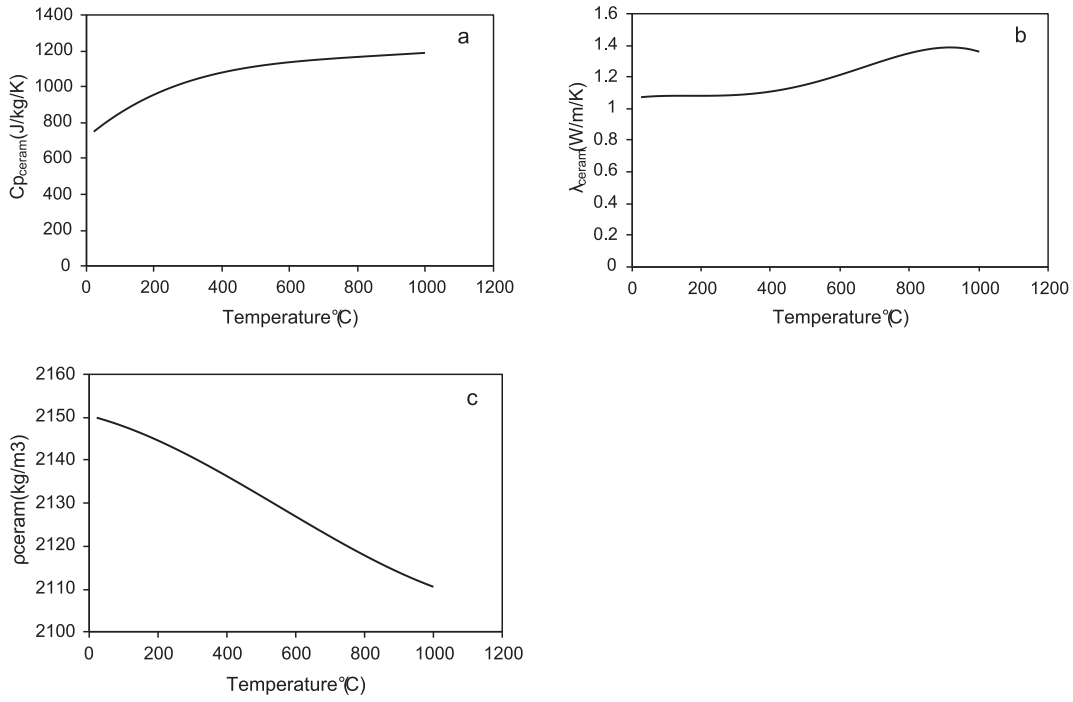

Fig. 1. Evolution of the fired ceramic thermophysical properties with temperature a) heat capacity (Cp), b) thermal conductivity (λ) and c) bulk density (ρ).

Table 1
Thermophysical properties of the fired ceramic.

X	a	b	c	d	e
$Cp_{ceram}\left(\frac{J}{kg \cdot K}\right)$	$-3957 \cdot 10^{-13}$	$1558 \cdot 10^{-9}$	$-2288 \cdot 10^{-6}$	$1597 \cdot 10^{-3}$	$7142 \cdot 10^{-1}$
$\lambda_{ceram}\left(\frac{W}{m \cdot K}\right)$	$-3 \cdot 10^{-12}$	$5 \cdot 10^{-9}$	$-2 \cdot 10^{-6}$	$3 \cdot 10^{-4}$	$1 \cdot 0661$
$\rho_{ceram}\left(\frac{kg}{m^3}\right)$	0	$3000 \cdot 10^{-11}$	$-5000 \cdot 10^{-8}$	$-2000 \cdot 10^{-5}$	2150.5

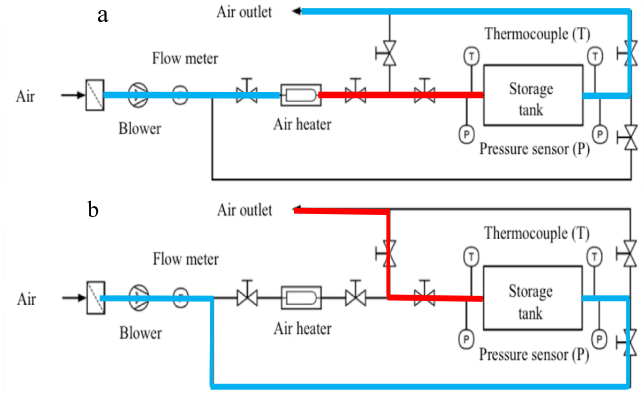

Fig. 2. Schematic of the present study experimental set-up. a) charging circuit and b) discharging circuit.

Prayon S.A company) and water. The mixture was prepared in a laboratory-type kneading bowl by mixing 95 wt% of raw clay extracted in the south of France and 5 wt% of hydroxyapatite. This was found as optimal composition according to our previous work [48]. Then, water (15 wt%) was added to the mixture, and the extrusion was performed at 8.0–9.0 bars pressure to obtain cylinders of approximatively 15 mm diameter and 20–30 cm length. These cylinders were subsequently dried in an electrical oven at 25 °C, 45 °C, 65 °C and 105 °C with a plateau time of 24 h at each temperature. Then, they were fired under the air in an industrial KILNOGY cell kiln (3 m^3) at 1140 °C for 1 h with a heating rate of 2 °C/min. After a natural cooling to room temperature, the fired

Table 2
Main characteristics of the TES pilot.

Parameters	Value	Unit
Nominal thermal storage capacity	34	kWh_{th}
HTF	Air	–
TES materials	Clay/phosphates-based ceramic	
Packed bed length, L	1.4	m
Packed bed height, H	0.3	m
Bed volume, V	0.126	m^3
Packed bed porosity, ε	0.41	–
Particles emissivity, e_s	0.91	–
Packed bed mass, m	162	kg
Tank walls thickness (vermiculite)	0.1	m
Tank coating thickness (rock wool)	0.25	m
Heat capacity of vermiculite	1000	J/kg/K
Thermal conductivity of vermiculite	0.15	W/m/K
Density of vermiculite	600	kg/m^3
Blower max delivered flow	305	m^3/h
Electrical heater power	30	kW
Maximum inlet temperature charging, T_H	900	°C
Minimun inlet temperature discharging, T_b	25	°C

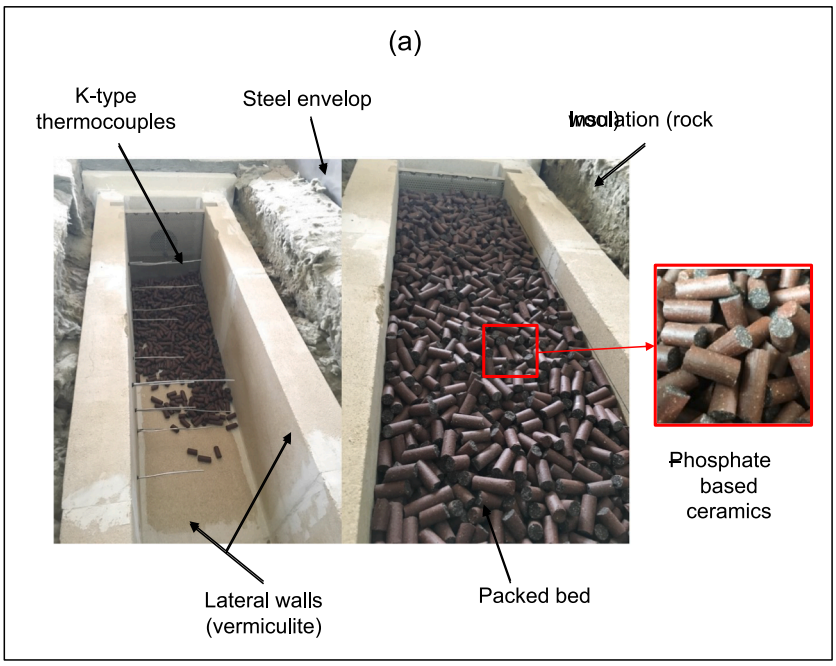

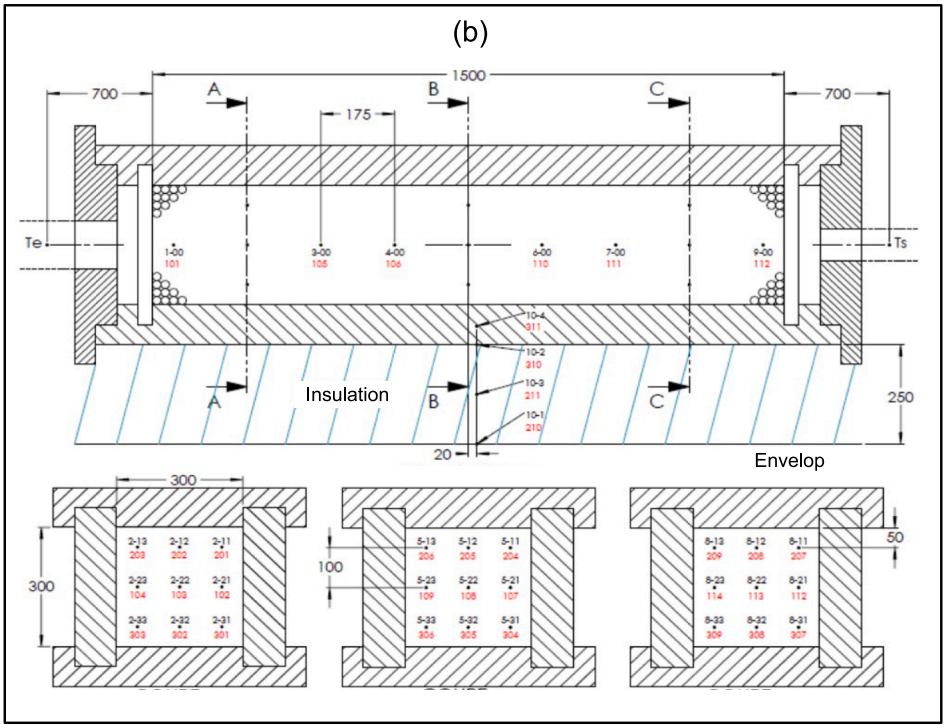

Fig. 3. A) photo of the packed bed storage tank during the filling with the fired ceramic; b) thermocouples position: x means the length from the top of the backed bed storage tank from the left-hand-side. Inside each section: the black dots indicate the positions of the thermocouples in each section, the red and the black numbers indicate the tags and the positions of the thermocouples. (For interpretation of the references to colour in this figure legend, the reader is referred to the web version of this article.)

phosphate-based products were cut to reach the final shape (cylinders of 15 mm diameter and 40 mm length, as illustrated in (Fig. 3 a).

The thermo-physical properties of the phosphate-based ceramics were evaluated from room temperature to 1000 °C. The heat capacity of the fired ceramic (C_p) was measured using a differential scanning calorimetry with a DSC 404 F1 Pegasus®. The measurement was carried out in a dynamic argon atmosphere (gas flow rate: 50 NmL/min) from room temperature to 1000 °C with a heating rate of 20 °C/min.

The thermal diffusivity (φ) was measured by Laser Flash technique in a NETZSCH laser flash apparatus (LFA 467 HyperFlash@) from room temperature to 1000 °C. The thermal conductivity (λ) was then deduced as described in our previous work [48].

The bulk density (ρ) was measured at room temperature using a water absorption technique described in our previous study [48].

Table 3
Characteristic parameters for calculating the properties of the air as a function of the temperature.

X	a	b	c	d	e
$Cp_{air}\left(\frac{J}{kg\cdot K}\right)$	$2.42.10^{-10}$	$-7.131\cdot10^{-7}$	$6.581\cdot10^{-4}$	$-8.615\cdot10^{-3}$	1006
$\lambda_{air}\left(\frac{W}{m\cdot K}\right)$	0	$9.38\cdot10^{-12}$	$-2.592\cdot10^{-8}$	$7.298\cdot10^{-5}$	$2.477\cdot10^{-2}$

The thermal dimension variation of the fired material was performed in a TMA 1600 SETERAM dilatometer from room temperature to 1000 °C (5 °C/min heating rate).

The thermogravimetry analysis of the fired material was carried out in a Q600 apparatus (TA Instruments) from room temperature to 1000 °C (5 °C/min heating rate).

Then, from the density determined at room temperature, and the variation of mass and dimension as a function of the temperature, the density of the fired ceramic could be calculated from room temperature up to 1000 °C.

From the results obtained, the expressions of C_p, λ, and ρ, as a function of the temperature could be deducted according to the Eq. (1), plotted in the Fig. 1.

$$\boldsymbol{X} = \boldsymbol{aT}^4 + \boldsymbol{bT}^3 + \boldsymbol{cT}^2 + \boldsymbol{dT} + \boldsymbol{e} \quad (1)$$

The characteristic parameters of the Eq. (1) to calculate **X** are summarized in Table 1.

2.2. Thermocline TES pilot description

Fig. 2 shows a scheme of the pilot used for TES tests, which includes a packed bed storage tank, a fan blower, an electric heating generator (30 kW power, SureHeat Max HT) and an insulated pipeline circuit. This apparatus allows performing either single charge or discharge, or several consecutive charge–discharge cycles.

During the charging process (Fig. 2 a), hot HTF (i.e. air) heated up to 900 °C passes throughout the storage tank and transfers heat to the filler material, up to a defined threshold temperature.

For the discharging step (Fig. 2 b), ambient air, at a constant mass flowrate using a fan blower (SCL K06) equipped with a frequency converter, is injected in the opposite direction of the charge to generate the useful recovered energy (hot air). A DELTAFLOWC flow meter located after the fan blower was used to measure the air mass flow with respect to the temperature of the fluid with an accuracy of ± 4 %. The signals are monitored with a Graphical User Interface developed using the LabVIEW software.

Table 2 shows the characteristics of the TES pilot. The dimension of the packed bed is 1.4 m length, 0.3 m width, and 0.3 m height, leading to a total storage volume of 0.126 m^3. The walls of the pilot were built by vermiculite material (10 cm thickness), insulated by a rock wool (25 cm thickness), and mechanically protected by a stainless-steel shell (Fig. 3a). The total storage volume of the tank allows calculating a nominal maximal thermal storage capacity of 34 kWh_{th} if it is filled with the developed materials and charging temperature of 900 °C. In this study, it is fulfilled with 162 kg of the fired clay/phosphate ceramic presented above (cylinders of 1.5 cm diameter and 4 cm length), leading to the void fraction of the packed bed of *ca.* 40 %, which was calculated from the mass and the density of the ceramic, and the total volume of the TES tank. The axial and radial temperature profiles inside the storage tank are carefully monitored using a series of 33 K-type thermocouples implemented along the tank and in the insulation wall as shown in Fig. 3b. Nine thermocouples implemented in the centerline of the tank from the left to the right record the axial temperature profile. Radial temperature distribution is monitored within three sections A, B, C. The section A, which was found at 0.225 m from the top of the storage tank from the left-hand-side, was composed of nine thermocouples, 8 of them were located at 5 cm far from the tank wall, while the 9th one was set at the center of the section. The sections B and C, which were found at 0.75 and 1.275 m from the top of the storage tank from the left-hand-side, also contained 9 thermocouples each, with the same configuration as for those of the section A. All the thermocouples are calibrated in the temperature range of 25–900 °C with an uncertainty of ± 1 °C.

Four more thermocouples are placed respectively in the vermiculite wall, between the vermiculite and the rock wool, in the center of the insulation and close to the steel wall.

2.3. Experimental investigations

Charge and discharge tests were performed with the fulfilled pilot.

For these tests, temperature thresholds (cut-off temperatures) have been chosen to evaluate performances. These temperatures depend on a threshold coefficient, β, which has been arbitrarily defined according to Eq. (2) and Eq. (3).

$$\boldsymbol{T_{ch,thr}} = \boldsymbol{T_b} + \boldsymbol{\beta}\cdot(\boldsymbol{T_H} - \boldsymbol{T_b}) \quad (2)$$

$$\boldsymbol{T_{dis,thr}} = \boldsymbol{T_b} + (1-\boldsymbol{\beta})\cdot(\boldsymbol{T_H} - \boldsymbol{T_b}) \quad (3)$$

During a typical charge, when the outlet temperature (T_{out}) increases and reaches the charge temperature threshold ($T_{ch,thr}$), the charge is stopped. Similarly, during a typical discharge, when the outlet temperature decreases and reaches the discharge temperature threshold ($T_{dis,thr}$), the discharge is stopped.

Temperature thresholds enable the estimation of different parameters used to evaluate the performance of the thermocline TES including the load rate (η_{ch}), the discharge rate (η_{dis}), the thermocline thickness (H_{tc}), the ratio of energy wasted at the outlet of storage not recovered (η_{out}) and the energy losses through the walls ($E_{wall,loss}$).

- The load rate (η_{ch}), which is calculated by Eq. (4), is the ratio between the charged energy when the defined threshold is reached ($E_{ch,thr}$), and the maximum energy that could be charged in the storage media (E_{max}). This ratio corresponds to the final state of the charge and considers the thermal gradient in the storage tank. $E_{ch,thr}$ and E_{max} are calculated according Eq. (5) and Eq. (6) where Cp_{ceram} is specified in Table 1.

$$\eta_{ch} = \frac{E_{ch,thr}}{E_{max}} \quad (4)$$

$$E_{ch,thr} = \sum_{i=1}^{n} \frac{m}{n} \int_{T_{amb}}^{T_{ch,thr}} Cp_{ceram}(T)dT \quad (5)$$

$$E_{max} = m\cdot Cp_{ceram}(T_H - T_b) \quad (6)$$

- The discharge rate (η_{dis}), which is calculated by Eq. (7) corresponds to the ratio between the energy that has been discharged ($E_{dis,thr}$) and the energy that has been charged in the storage tank before starting the discharge step ($E_{initially,\ ch}$). $E_{dis,thr}$ is calculated from the beginning of the discharge to the moment where the $T_{dis,thr}$ is reached (Eq. (8)). For the calculation of $E_{dis,thr}$, the properties of the air is provided by Eq. (9) and Table 3.

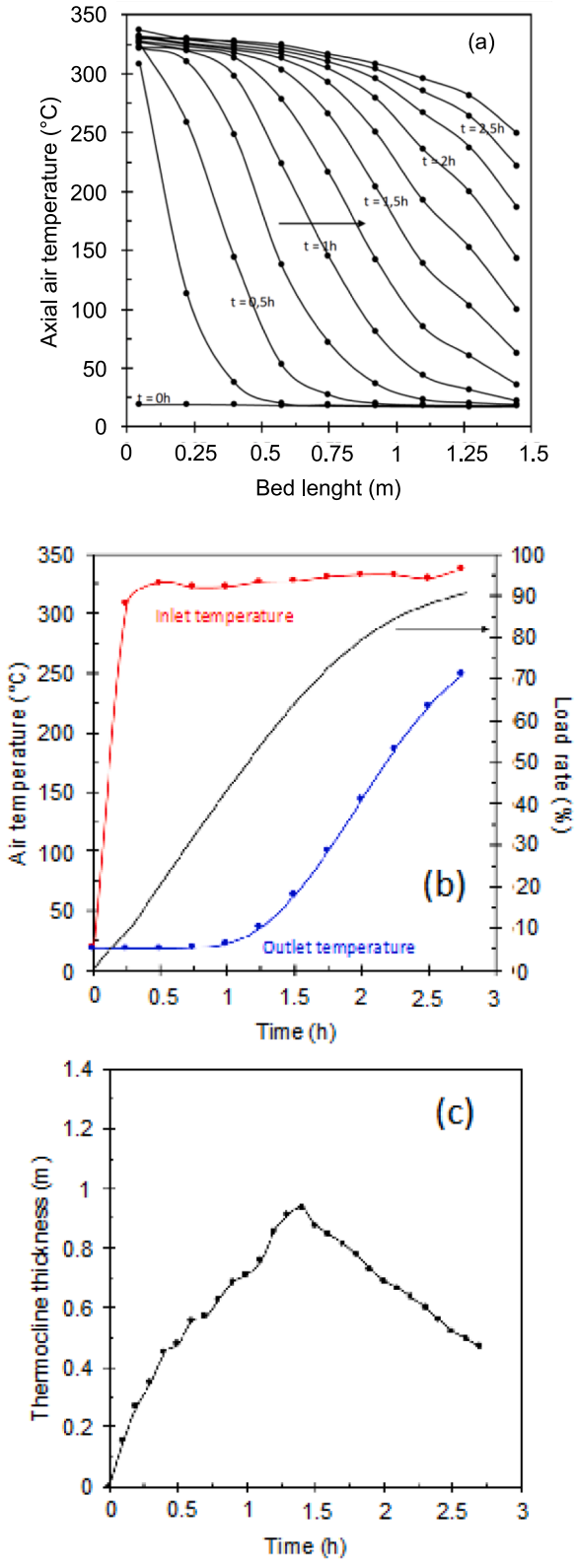

Fig. 4. A) axial air temperature distribution along the bed; b) inlet and outlet temperature, and load rate during the charging phase; c) Thermocline thickness evolution with the charging time.

Table 4
Indicators of the storage performances at different threshold coefficients.

Threshold coefficient, β (%)	20	40	60
Threshold temperature, $T_{ch,thr}$ (°C)	83	146	209
E_{in} (kWh)	10.78	13.25	15.72
$E_{ch,thr}$ (kWh)	10.30	11.91	12.97
Charge duration, $t_{ch,thr}$ (h)	1.65	2.02	2.41
η_{ch} (%)	69.20	80.10	87.20
η_{out} (%)	3.10	7.70	14.30
$H_{tc,max}$ (m)	0.93		
$E_{wall,loss}$ (kWh)	0.14	0.32	0.50

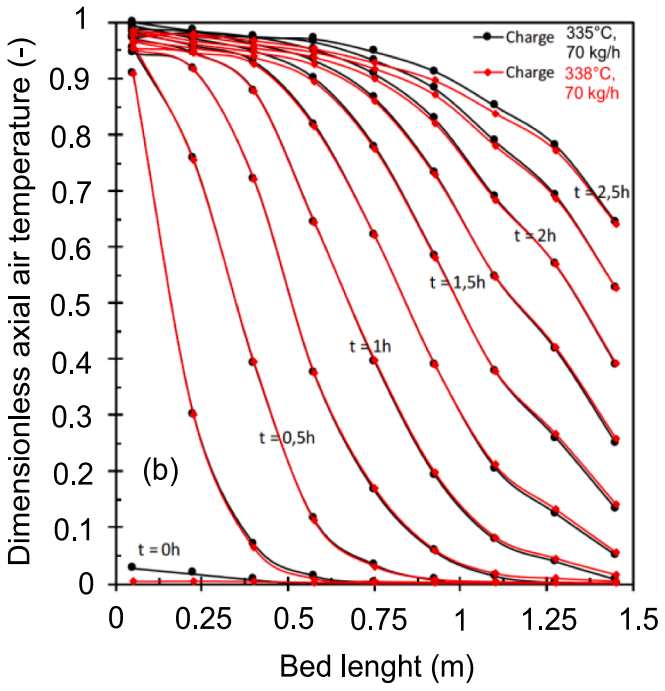

Fig. 5. Reproducibility test of charging phase.

$$\eta_{dis} = \frac{E_{dis,thr}}{E_{initiallych}} \tag{7}$$

$$E_{dis,thr} = \int_0^{t(T_{dis,thr})} \dot{m}_{air} \cdot Cp_{air}(T_{out} - T_b)dt \tag{8}$$

$$X = aT^4 + bT^3 + cT^2 + dT + e \tag{9}$$

- The quantity of heat dissipated at the outlet and not stored in the tank (E_{out}) was evaluated using Eq. (10). Finally, the rate of energy loss (η_{out}) is defined by Eq. (11) where E_{in} is the energy of the air at the inlet at a given time calculated using Eq. (12).

$$E_{out,thr} = \int_0^{t(T_{ch,thr})} \dot{m}_{air} \left(\int_{T_{amb}}^{T_{out,thr}} Cp_{air} dT \right) dt \tag{10}$$

$$\eta_{out} = \frac{E_{out}}{E_{in}} \tag{11}$$

$$E_{in,thr} = \int_0^{t(T_{ch,thr})} \dot{m}_{air} \left(\int_{T_{amb}}^{T_{in,thr}} Cp_{air} dT \right) dt \tag{12}$$

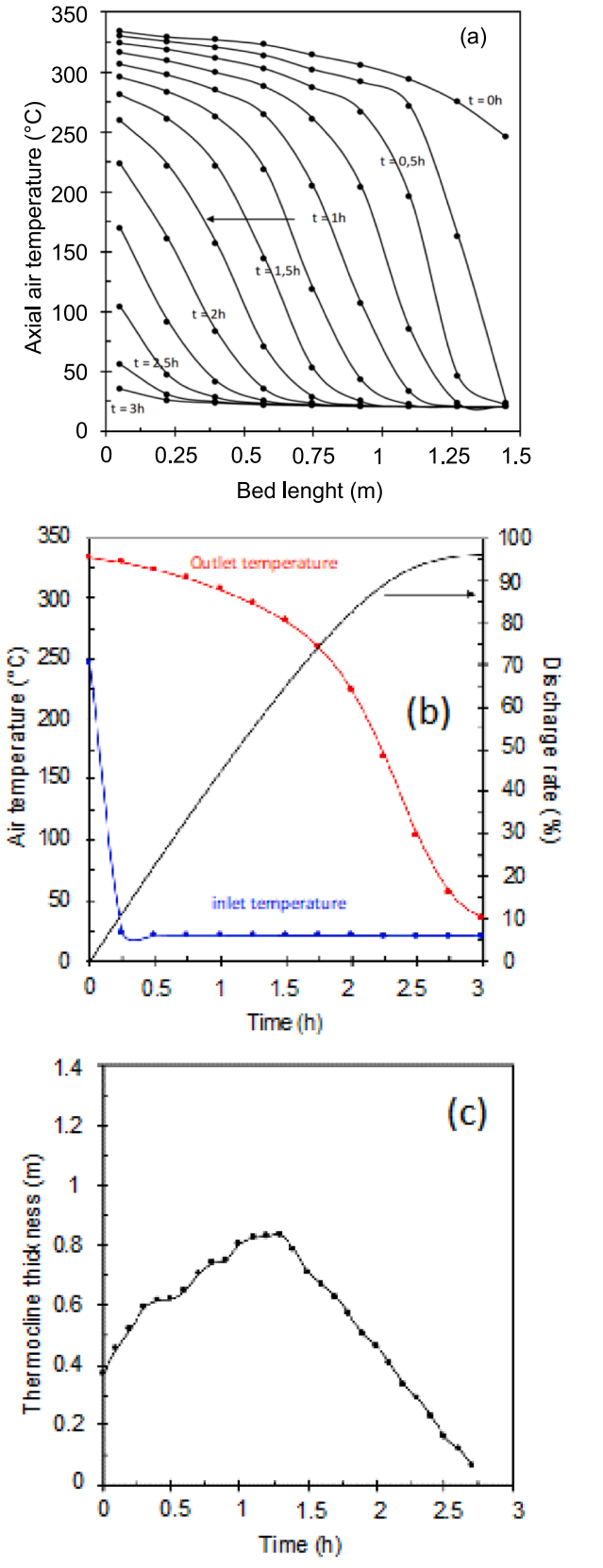

Fig. 6. A) temperature profiles at the centerline of the air; b) Inlet, outlet temperatures and discharge rate during the discharging phase; c) Thermocline thickness evolution during the discharging phase.

Table 5
Indicators of the storage performances for different threshold coefficients.

Threshold coefficient, β (%)	20	40	60
Threshold temperature, $T_{dis,thr}$ (°C)	272	209	146
$E_{diss,thr}$ (kWh)	9.38	11.45	12.27
Discharge duration, t_{thr} (h)	1.61	2.07	2.34
η_{diss} (%)	69.40	84.60	90.70
H_{tc} (m)	0.84		

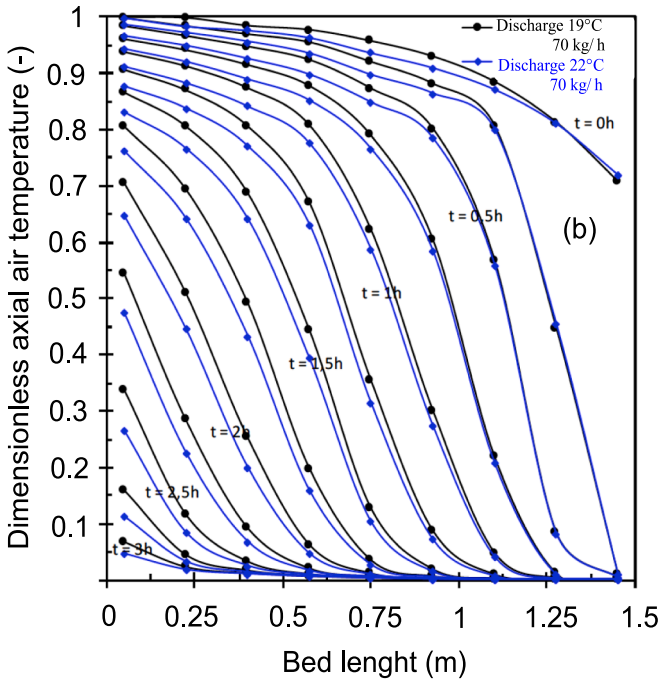

Fig. 7. Reproducibility test of the discharging phase.

- The heat loss through the walls was then calculated using Eq. (13) only during the charging phase.

$$E_{wall\_loss,thr} = E_{in,thr} - E_{chr,thr} - E_{out,thr} \tag{13}$$

- The thermocline thickness (H_{tc}) represents the thickness of the thermal gradient in the storage tank. It is defined as the part of the tank in which the temperature is between two thresholds (β = 0.9 and 0.1). It is evaluated by Eq. (14), as already reported in many scientific studies [49 50].

$$H_{tc} = \begin{cases} H_{T_{90\%}} - H_{T_{10\%}} \ \ if\ T_{in} \leqslant T_{10\%} and\ T_{out} \geqslant T_{90\%} \\ H_{T_{90\%}} - 0 \ \ if\ T_{in} > T_{10\%} \\ H - H_{T_{10\%}} \ \ if\ T_{out} < T_{90\%} \end{cases} \tag{14}$$

- Recovered thermal power (P_{th}):

$$P_{th} = E_{diss}/t\left(T_{dis,thr}\right) \tag{15}$$

- Global efficiency of a given storage cycle ($Eff_{overall}$):

$$Eff_{overall} = \eta_{dis} \cdot \eta_{ch} \tag{16}$$

3. Results and discussions

3.1. Description of a typical charge

Fig. 4 a shows the axial air temperature evolution along the storage

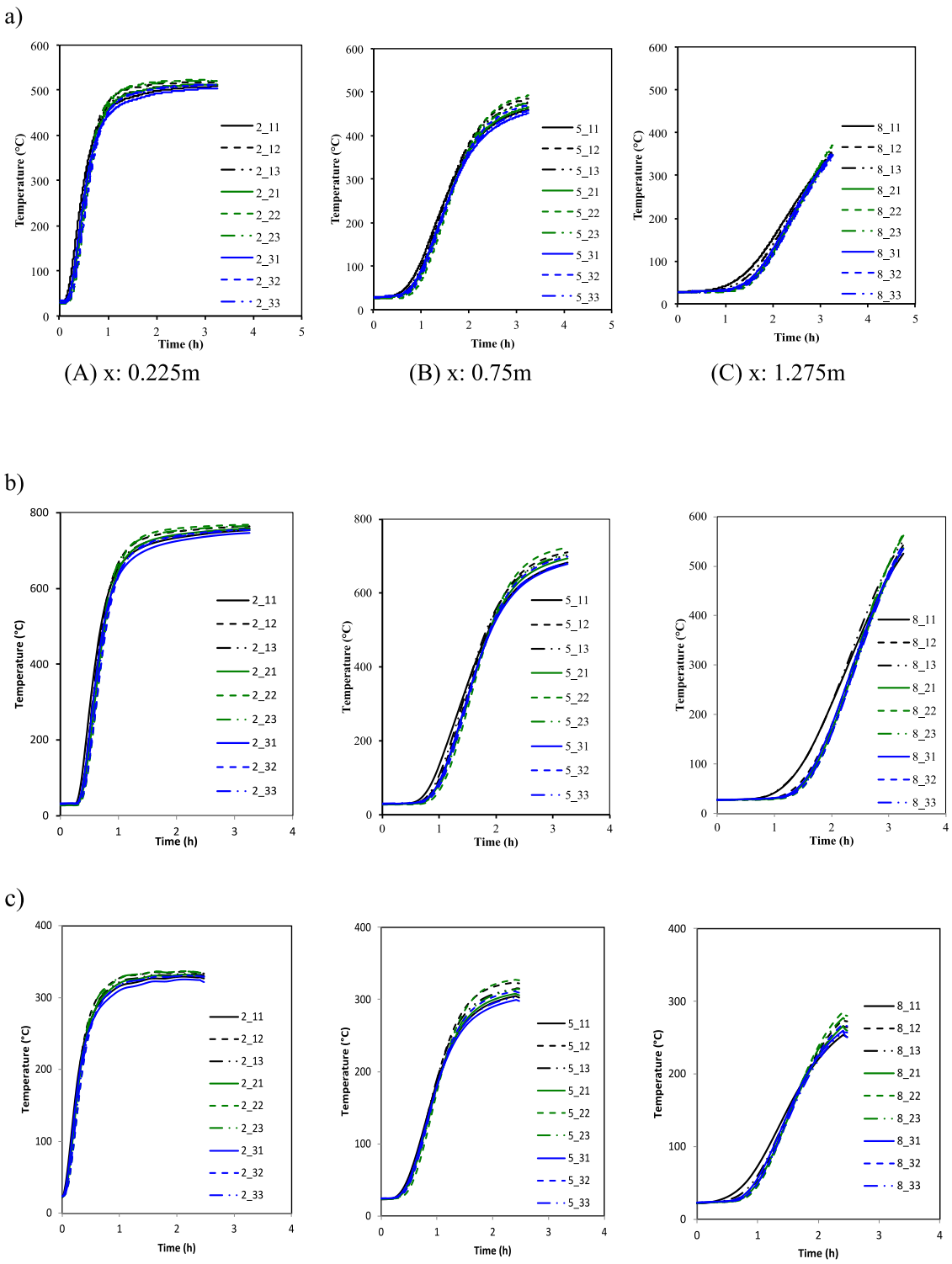

Fig. 8. Radial temperature profiles inside the packed bed during a charging step with the hot inlet air at a) 535 °C and at the flowrate of 49.5 kg/h; b) 775 °C and the flowrate of 57 kg/h; c) 343 °C and the flowrate of 74 kg/h.

medium pictured every 0.25 h during the first full charge, using hot air at 335 °C with a mass flowrate of 70 kg/h. At the beginning of the charge (t = 0h), the temperature of the full storage medium reached $T_b = 24$ °C. The inlet temperature was quickly stabilized at 335 °C after 0.25 h and remained stable during the test (Fig. 4 b). The charge is stopped after 2.75 h with a storage packed bed average temperature around 300 °C, when the temperature of the outlet air reached trhe threshold ($T_{ch,thr}$ = 265 °C, Fig. 4 b).

It can be observed that for a selected charging time, the axial temperature decreases by increasing the length of the bed; which shows the thermocline evolution within the tank, *i.e.* the slope between a hot and a cold zone. A perfect charge would give a vertical slope between the zones with a homogeneous high and cold temperature. The observed slope is due to the non-perfect heat exchange between air/ceramics and the thermal diffusion in the packed bed.

Fig. 4 c shows the evolution of the thermocline thickness during the

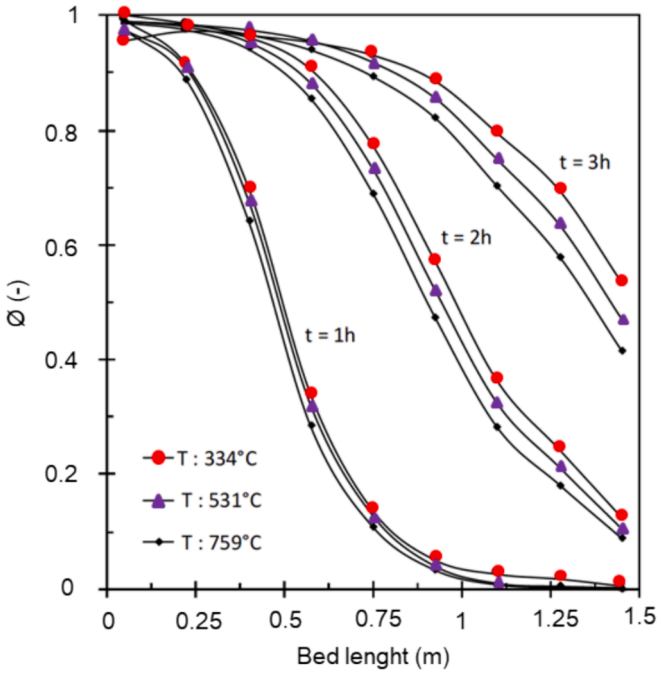

Fig. 9. Dimensionless axial air temperature distribution along the storage tank during the charge by different hot inlet air temperature of 334 °C, 531 °C and 759 °C; mass flowrate of 48 +/- 2 kg/h.

charging time. At t = 0h, the thermocline thickness is 0 m. Within 0–0.5 h of charge, the thermocline was formed and its thickness quickly increased to reach *ca.* 0.48 m. Then, the thermal diffusion and the non-perfect exchange air/packed bed induced the expansion of the thermocline within 0.5–1.4 h of charge. At 1.4 h of charging time, a maximum thickness was found at *ca.* 0.94 m, representing 67 % of the packed bed zone. Then, this thickness decreased with the time up to 0.45 m at the end of the charge (t = 2.75 h). In fact, after reaching the maximum value (at t = 1.4 h), the thermal gradient got out of the tank leading to the increasing of the outlet temperature as presented in Fig. 4 b.

In Fig. 4 b, the load rate (η_{ch}, Eq. (4)) increased with the charging time as expected. At the end of the charge, when the outlet air reached the threshold ($T_{ch,thr}$ = 265 °C), the load rate reached 90 %. Generally, the load rate can vary, depending on the properties of the filler medium, but also on the selected threshold temperature, or the threshold coefficient (β, see Eq. (2). In this study, the impact of this threshold coefficient was investigated between 20–60 %. Different charging tests were done (results not shown) and Table 4 summarizes the results for threshold coefficient of 20 %, 40 % and 60 %. Thus, increasing the threshold coefficient (which leads to increasing threshold temperature) allowed increasing the load rate (η_{ch}). However, this also led to an increase of the rate of energy loss (η_{out}). In the case of the fired clay/phosphate-based ceramic, for a high threshold temperature of 209 °C in comparison with the inlet hot air temperature of 335 °C, the rate of energy loss (η_{out}) of 14.30 % is acceptable, showing the high performance of the developed material to store heat.

To illustrate the reproducibility of the charging step, a second charging test was carried out under the similar conditions (T_H=335 °C, air mass flow of 70 kg/h). The results are presented in Fig. 5, showing the perfect repeatability of the charge using the fired clay/phosphates-based ceramic.

As partial conclusion, the studied TES system filled with the fired clay/phosphate-based ceramic can be advantageously used to collect heat with high reliability. The thermocline storage effectiveness during a typical charge strongly depends on the defined threshold coefficient and therefore on the operating conditions. It is essential to know the behavior of the whole system in which the storage system is connected to evaluate the optimal threshold.

3.2. *Typical discharge description*

After the charging phase (Fig. 4), the system was immediately discharged with the cold air (ambient temperature, *ca.* 25 °C, flowrate of 70 kg/h), which was injected from the right-hand-side of the tank (opposite side of the charging phase). Fig. 6 a shows the evolution of the temperature along the storage tank at different discharging times, while the inlet and outlet temperature of the hot air is displayed in Fig. 6 b. As

Table 6
Load rate, charge duration, thermocline thickness for a charging temperature of 334 °C, 531 °C and 759 °C with a threshold coefficient of 60 %.

$\dot{m}$(kg/h)	T_H (°C)	$T_{ch,thr}$ (°C)	t_{thr} (h)	$E_{ch,thr}$ (kWh)	E_{max} (kWh)	$\eta_{ch,thr}$ (%)	$\eta_{out,thr}$ (%)	$H_{tc,\ max}$ (m)	Δp (Pa)
48	334	216	3.15	12.80	14.80	86.70	17.60	1	181
49.5	531	329	3.46	22.10	25.23	87.60	14.30	0.96	376
48	759	466	3.76	32.90	37.81	86.90	13.80	0.96	450

Table 7
Effect of the charging air mass flow; Experimental working conditions and results for different inlet temperature. (A): 334 +/- 21 °C; (B): 531 +/- 23; (C): 760 +/- 15.

(A)	Charging conditions T_H(°C)	$\dot{m}$(kg/h)	$T_{ch,thr}$ (°C)	t_{thr}(h)	$E_{ch,thr}$ (kWh)	$\eta_{ch,thr}$(%)	$H_{tc,max}$(m)	η_{out}(%)	Δp (Pa)
Test 1	334 +/- 21	48	215	3.24	12.85	86.70	1.00	17.60	181
Test 2		66.5	224	2.57	13.73	87.10	0.97	15.80	341
Test 3		70	210	2.44	13.31	87.40	0.95	15.50	370
Test 4		74	214	2.28	13.27	86.90	0.91	14.10	430
(B)	Charging conditions T_H(°C)	$\dot{m}$(kg/h)	$T_{ch,thr}$(°C)	t_{thr}(h)	$E_{ch,thr}$ (kWh)	$\eta_{ch,thr}$(%)	$H_{tc,max}$(m)	η_{out}(%)	Δp (Pa)
Test 5	531 +/- 23	49.50	329.40	3.46	22.14	87.12	0.96	14.30	329
Test 6		55	345.10	3.14	22.82	88.10	0.93	14.60	376
Test 7		66	331.60	2.79	22.83	87.80	0.91	14.20	484
(C)	Charging conditions T_H(°C)	$\dot{m}$(kg/h)	$T_{ch,thr}$(°C)	t_{thr}(h)	$E_{ch,thr}$ (kWh)	$\eta_{ch,thr}$(%)	$H_{tc,max}$(m)	η_{out}(%)	Δp (Pa)
Test 8	760 +/- 15	48	465.60	3.76	32.90	86.90	0.96	13.90	449
Test 9		57	475.80	3.25	33.90	87.20	0.92	12.90	498

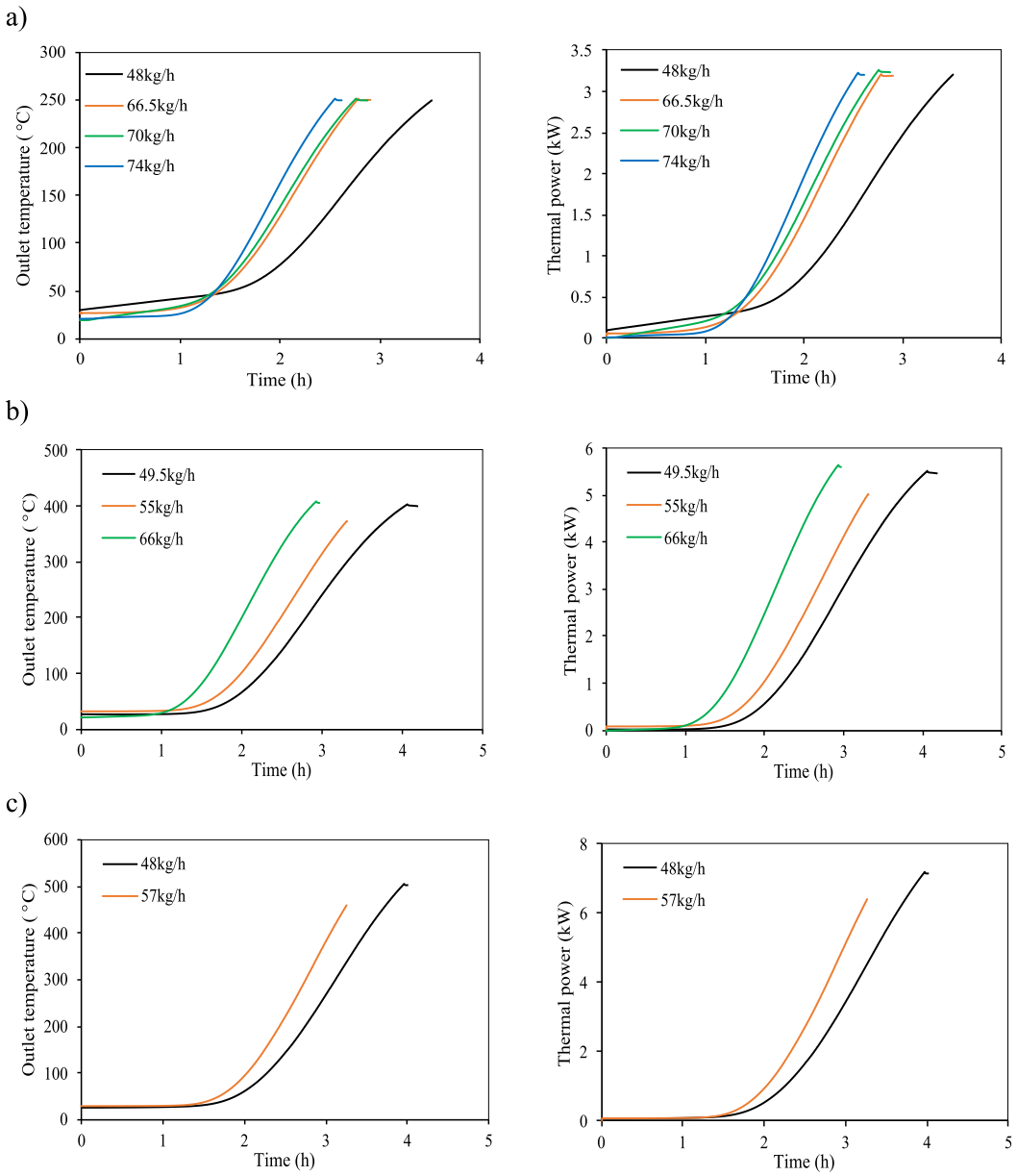

Fig. 10. Effect of the charging air mass flow; Outlet temperature and thermal power as function of time for different inlet temperature. (a): 334 +/- 21 °C; (b): 531 +/- 23; (c): 760 +/- 15.

expected, at a given discharging time, the temperature of the filler material decreased from the injection side to the outlet side (Fig. 6 a). In parallel, the inlet temperature quickly decreased to the room temperature and remained stable along the discharge, and the outlet temperature progressively decreased up to the room temperature at the end of the discharge (Fig. 6 b). It is worth noticing that due to the thermal losses (wall losses), the outlet temperature could not reach a plateau along the discharging phase. It strongly decreased after 1.25 h when the thermocline was extracted. As consequence, the discharge rate (η_{dis}, Eq. (7)) quickly increased during the first 2.5 h of discharge before gradual tapering. The first half of stored heat could be discharged within the first hour at the highest temperatures. At the end of the discharge, all the energy stored by the clay/phosphates-based ceramic bed was released and the discharge rate is close to 1 (Fig. 6 b). As observed for the charging phase, the thermocline thickness passed through a maximum of 0.83 m (59 % of the storage bed length) at 1.25 h of discharge before decreasing until the complete discharge of the system (Fig. 6 c).

The impact of the threshold coefficient (β, Eq. (3)) during the discharge was also investigated. Table 5 compares the discharge duration, the discharge rate and heat losses calculated for different arbitrary threshold temperatures. For low threshold coefficient of 20 %, corresponding to an application case which requires heat above 270 °C, 69.5 % of the stored energy can be recovered during with 1.61 h of discharging time. By decreasing the threshold temperature, the discharge rate logically increased.

The repeatability of the discharge was also verified. Fig. 7 shows that the discharging step was relatively well repeated when it the conducted twice under the similar conditions.

3.3. Homogeneity of air flow during a typical charge

As mentioned before, 27 thermocouples were implemented within 3 sections A, B, C (9 thermocouples for each section) for the monitoring of the temperature inside the storage tank (Fig. 3). As an example, Fig. 8 a shows the evolution of the radial temperature of each section during the charge using inlet hot air at 531 °C temperature and 49.5 kg/h flowrate.

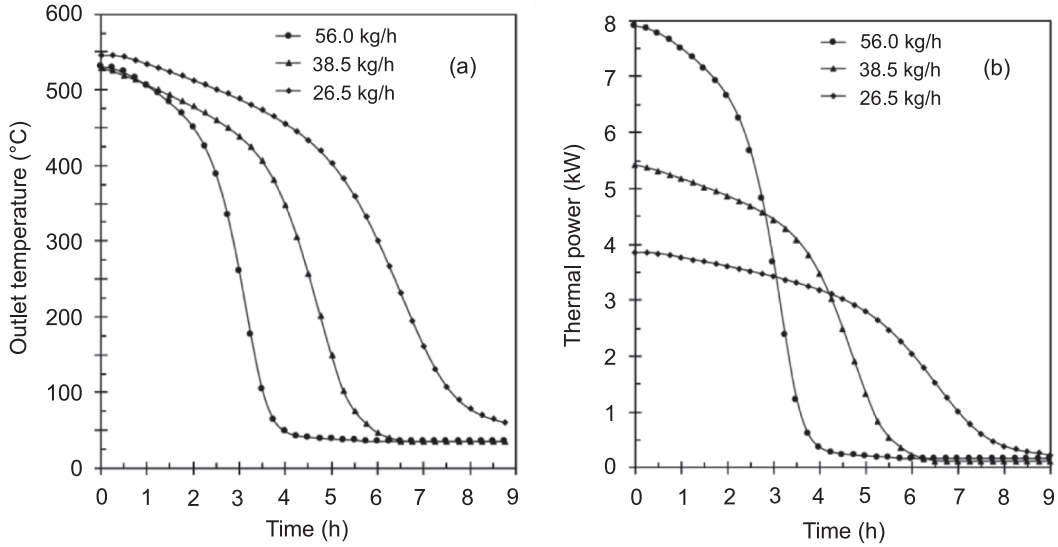

Fig. 11. A) outlet temperature and b) output power as function of time at 26.5, 38.5 and 56 kg/h discharge flow rate.

Table 8
Effect of the discharging air mass flow; Experimental working conditions and results for a threshold coefficient (β = 0.6).

Test	Discharging conditions			P_{th}-max (kW)	t_{thr}(h)	η_{diss}(%)	$H_{tc,max}$(m)
	$\dot{m}$(kg/h)	T(°C)	$T_{dis,thr}$(°C)				
1	26.50	25 °C	400	3.80	5.05	90.30	1.10
2	38.50	+/-5		5.40	3.55	94.40	1
3	56			7.90	2.42	91.20	0.86

During 3 h of charge, the radial temperature profile was practically homogeneous for each section, which proves there is no significant preferential path of the hot air inside the storage medium. This behavior was also observed for the charging steps under other conditions (Fig. 8 b and c). This strongly answers to the requirement for a suitable operation of a thermocline TES system. Similar behavior could also be observed for the discharging step (see Figures SI 1, SI 2 and SI 3 in Supporting Information). Thus, we can conclude that both the horizontal position of the storage tank and the cylindrical shape of the extruded fired clay/phosphate ceramic developed in this work did not generate a notable preferential flow in the storage medium and did not create enough thermal stratification during the charging and discharging phases, proving the high potential of application of this material at the industrial scale.

3.4. Effect of the charging temperature

Fig. 9 shows the axial air temperature profile along the packed bed recorded during the charging step with three different temperatures of the hot inlet air (334 °C, 531 °C and 759 °C) and with the same mass flowrate of 48 +/- 1.5 kg/h.

To compare the three experiments, the dimensionless axial air temperature profiles were used. At 1 h of charging time, the profiles were similar to each other along the storage bed. At 2 and 3 h of charging time, the dimensionless axial air temperature inside the packed bed was only slightly lower when the temperature of the hot inlet air was higher. This means that the thermocline was extracted more quickly for low inlet temperature and the wasted heat at the outlet was higher. The slight difference in the dimensionless axial air temperature distribution shown in Fig. 9 can be explained by considering the variation of the thermal properties of the fluid and the packed bed with the temperature. Keeping stable the hot inlet air at high temperature led to more energy, which was lost by being stored in the wall of the tank. Accordingly, as shown in Table 6, for the same threshold coefficient (β, Eq. (2)) of 60 % representing a relative deep charge of the system, the charge duration slightly increased when increasing the temperature of the hot inlet air. Nevertheless, there was not any notable influence on the load rate and the thermocline thickness. However, the pressure drop notably increased; explained by the evolution of the air thermophysical properties with the temperature leading to a significant velocity increase through the packed bed. This pressure drop increase requires more energy for the auxiliary (pumping energy). On the other hand, this allows storing more thermal energy ($E_{ch,thr}$, Table 6).

Hence, as partial conclusion, the thermocline TES system filled with the fired clay/phosphate-based ceramic can be advantageously used in a large range of heat sources.

3.5. Influence of the charge / discharge air mass flowrate

3.5.1. Charging phase

The effect of the inlet air mass flowrate during the charge was studied by keeping the inlet temperature relatively stable, and varying the air mass flowrate. The performance of the storage was then evaluated by fixing an arbitrary threshold coefficient (β = 0.6). The experimental working conditions and the results are summarized in Table 7 and Fig. 10.

Table 7 A and Fig. 10 a shows the results obtained with the inlet air temperature of 334 +/- 21 °C. As expected, the increase of the inlet air mass flowrate allowed reducing the charging time (t_{thr}), the energy loss rate (η_{out}) and the outlet thermal power. Furthermore, it provoked an increase of the pressure drop inside the storage tank. On the other hand,

Table 9
Experimental working conditions used for consecutive charge/discharge cycles.

Charge				Discharge			
Inlet temperature, (°C)	Air flowrate (kg/h)	$T_{thr,ch}$(°C)	β (%)	Inlet temperature, (°C)	Air flowrate (kg/h)	$T_{thr,dis}$(°C)	β (%)
576	60	113	15	*ca.* 25 °C	60	498	15

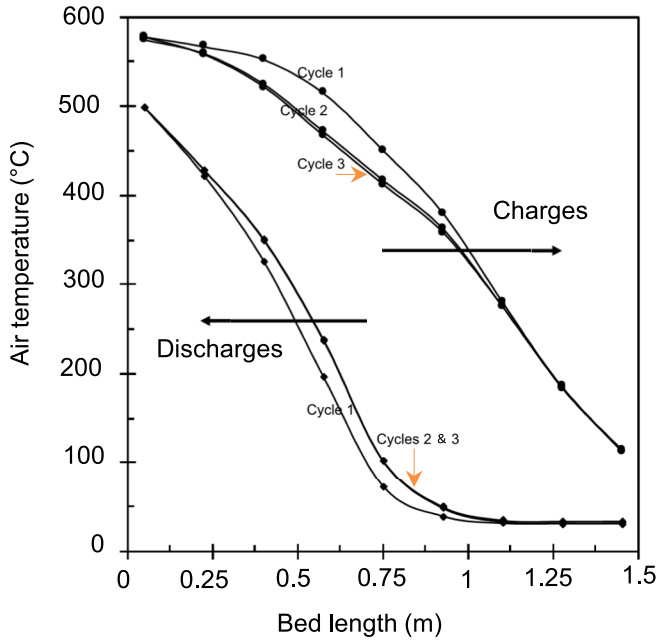

Fig. 12. Axial temperature profiles along the packed bed pictured at the end of the charge and discharge phases during the continuous operation.

the inlet air mass flowrate had no significant impact on the load rate ($\eta_{ch,thr}$, *ca.* 87 %) and the maximal thermocline thickness ($H_{tc,max}$, *ca.* 0.9–1.0 m).

Low mass flowrate leads to increases the residence time of the air in the bed which means higher temperature gradients due to a low heat transfer through convection between the air and the filler material, the thermal diffusion and then higher thermal losses at the outlet of the tank.

3.5.2. Discharging phase

The impact of the air mass flowrate on the TES system performances was also investigated by varying the discharge flowrate within 26.5–56 kg/h; the inlet temperature and the final load rate of the charging phase being kept constant at 25 °C +/-5 and $\beta = 0.6$, respectively.

As expected, the increase of the discharging air flowrate allowed accelerating the discharge of the storage tank, as illustrated by the outlet air temperature and the recovered thermal power in Fig. 11. Thus, at the discharging air flowrate of 26.5 kg/h, more than 9 h is necessary to completely discharge the tank (outlet air temperature at around 50 °C), whereas this time decreased to *ca.* 6.5 and 4.5 h at 38.5 and 56 kg/h, respectively (Fig. 11 a). Consequently, the profile of the recovered thermal power (P_{th}, Eq. (15)) was strongly impacted as illustrated in Fig. 11 b. At high discharging flowrate, P_{th} started at a high value (7.9 kW) and quickly decreased due to the fast decrease of the outlet temperature. This means most of the stored heat was extracted at the beginning of the discharge. In contrast, at lower discharging flowrate, P_{th} started at lower values (5.4 and 3.8 kW at 38.5 and 26.5 kg/h, respectively), and the extraction of the stored heat needed more time since the heat transfer between the air and the filler material is low. Regarding now other parameters, at the same threshold coefficient ($\beta = 0.6$), the discharge rate (η_{diss}) was practically unchanged which reached 90.3–94.4 % as shown in the Table 8. However, the maximal thermocline thickness ($H_{tc,max}$) slightly increased from 0.86 m at 56 kg/h to 1.1 m at 26.5 kg/h of discharging flowrate explained by the low velocity of air through the bed leading to a low convection heat exchange, an increase of the heat losses and the thermal diffusion. Thus, as partial conclusion, by modulating the discharging air flowrate, it is possible to control the output thermal power as a function of the downstream utilization without performances degradation, using clay/phosphate-based material developed in this work.

3.6. Continuous operation

To validate the robustness of the TES system, three consecutive charge/discharge cycles were performed. The experimental conditions are summarized in Table 9. In fact, during continuous operation, phenomenon such as natural convection is more likely to appear resulting in stratification of the thermocline.

Fig. 12 shows the temperature profiles along the packed bed for these three cycles pictured only at the end of each charge and discharge, when the outlet air temperature reach the corresponding threshold value ($T_{thr,ch}$ and $T_{thr,dis}$). The temperature profiles of the first cycle were slightly different from those of the second and the third cycles. Only a small destratification was observed between the cycles with a small decrease of the temperature slope, which suggests a good stability of the temperature profiles.

Table 10 summarizes the main characteristic parameters of the TES system during the consecutive cycles. Globally, as already observed in Fig. 12, apart a small variation between the first and the next cycles, all the parameters of the TES storage could be remained constant. These significant results prove the ability of the developed thermocline TES system to perform in continuous conditions, which suggests its high potential of application at the industrial scale.

4. Conclusions

The performances of a pilot scale storage packed bed system (useful tank dimension: 1.5 m × 0.3 m × 0.3 m) containing 162 kg of clay/phosphate-based ceramic material (cylinders of 1.5 cm × 4 cm) was experimentally investigated under different operating conditions of inlet air temperature for the charge (334 +/- 21 °C, 531 +/- 23 °C and 760 +/- 15 °C), charging and discharging air flowrate, as well as under consecutive cycle regime.

Salient conclusions arising from this study are summarized below:

- The cylindrical shape of clay/phosphate-based ceramic and the horizontal implementation of the storage tank did not provoke a significant preferential path for the air inside the storage medium, and did not create a thermal stratification during the charging and discharging phases.
- The storage packed bed performed well at different inlet air temperatures within *ca.* 334—760 °C, and different charging and discharging air flowrate (26.5 – 74 kg/h). In addition, under the

Table 10
Main indicators evaluated during a symmetrical charge and discharge of the storage system.

	Unit	Cycle 1		Cycle 2		Cycle 3	
	–	Charge	Discharge	Charge	Discharge	Charge	Discharge
T_{thr}	°C	113	498	113	498	113	498
t_{thr}	h	1.89	1.39	1.16	1.24	1.01	1.26
$\eta_{ch,thr}$	%	67	–	64	–	63.20	–
$\eta_{diss,thr}$	%	–	68	–	64	–	65
$Eff_{overall}$	%	45.50		41.00		41.20	
$H_{tc,max}$	m	0.98	1.00	1.11	0.95	1.15	0.95

continuous regime, the TES system could be quickly stabilized after the first cycle. This demonstrates the robustness and flexibility in the operation of the developed TES system, which can cover a wide range of application cases in the industry including waste heat recovery, grid services, CSP and hybrids power plants such CSP/PV/Wind.

This study opens new prospects for using the clay/phosphates-based ceramic to build new generation of robust, flexible, reliable, and cost-effective high temperature thermocline TES system for industrial assets decarbonation through renewable heat (high temperature) and/or electricity supply and supporting the high penetration of renewable sources into the grid. The availability of the developed ceramics at industrial scale worldwide provides an excellent opportunity for the effective commercialization of the TES technology.

Future work will focus on the economical evaluation and the validation of the long-term performances of this concept at the industrial scale with variable operating conditions and different heat transfer fluids.

CRediT authorship contribution statement

Abdoul Razac Sane: Writing – review & editing, Writing – original draft. **Nawal Semlal:** Supervision. **Rachid Boulif:** Supervision. **Claudia Toussaint:** Supervision. **Alain Germeau:** Supervision. **Ange Nzihou:** Supervision. **Doan Pham Minh:** Validation, Supervision.

Acknowledgments

The project was supported financially by PRAYON S.A, Belgium and OCP S.A, Morocco Companies. The support from ANRT, France is also acknowledged.

The authors would like to thank TERREAL Company for they technical help for ceramic production, and Eco-Tech Ceram (ETC) for the experimentations at the pilot scale.

Appendix A. Supplementary data

Supplementary data to this article can be found online at https://doi.org/10.1016/j.solener.2024.112799.

References

[1] Irena, Renewable Power Generation Costs in 2017, International Renewable Energy Agency, Abu Dhabi (2018).
[2] P. Li, Energy storage is the core of renewable technologies, IEEE Nanotechnol. vol. Mag. 2 (4) (2008) 13–18.
[3] K. Nithyanandam, R. Pitchumani, A. Mathur, Analysis of a latent thermocline storage system with encapsulated phase change materials for concentrating solar power, Appl. Energy 113 (2014) 1446.
[4] H. L. Zhang, J. Baeyens, J. Degrève and a. G. Cacères, "Concentrated solar power plants: Review and design methodology,," *Renewable and Sustainable Energy Reviews,* vol. 22, p. 466–481, 2013.
[5] D. Barlev, R. Vidu, P. Stroeve, Innovation in concentrated solar power, Sol. Energy Mater. Sol. Cells 95 (10) (2011) 2703–2725.
[6] T.M. Pavlovic, I.S. Radonjic, D.D. Milosavljević, L.S. Pantić, A review of concentrating solar power plants in the world and their potential use in Serbia, Renew. Sustain. Energy Rev. 16 (6) (2012) 3891–3902.
[7] D.M. Gonzalez, F. Dinter, Operability, Reliability and Economic Benefits of CSP with Thermal Energy Storage: First Year of Operation of ANDASOL 3, Energy Procedia 49 (2014) 2472–2481.
[8] S.E. Trabelsi, R. Chargui, L. Qoaider, A. Liqreina, A. Guizani, Techno-economic performance of concentrating solar power plants under the climatic conditions of the southern region of Tunisia, Ener Conv Manag 119 (2016) 203–214.
[9] Solar Millennium AG - Andasol 1 is officially inaugurated. [Online]. Available: http://www.solarmillennium.de/Press/Press_Releases/Andasol_1_is_officially_inaugurated,lang2,50,1660.html.. [Accessed 05 April 2019].
[10] NREL, "Concentrating Solar Power Projects - Andasol-2," [Online]. Available: https://www.nrel.gov/csp/solarpaces/project_detail.cfm/projectID=4.. [Accessed 05 April 2023].
[11] E. García, S. Relloso, Tower technology cost reduction approach after Gemasolar experience, Energy Procedia 69 (2015) 1660–1666.
[12] "Ressources et information concernant noorouarzazate Resources and Information," [Online]. Available: Available: http://www.noorouarzazate.com/. [Accessed 05 April 2023].
[13] NOOR ENERGY I. [Online]. Available: http://noorenergy.ae/a-about/. [Accessed 10 September 2023].
[14] V. M. B. Nunes, C. S. Queirós, M. J. V. Lourenço, F. J. V. Santos and C. A. N. d. Castro, "Molten salts as engineering fluids – A review: Part I. Molten alkali nitrates," *Applied Energy,* vol. 183, p. 603–611, 2016.
[15] Q. Peng, X. Yang, J. Ding, X. Wei and a. J. Yang, "Design of new molten salt thermal energy storage material for solar thermal power plant," *Applied Energy,* vol. 112, p. 682–689, 2013.
[16] A. Caraballo, S. Galán Casado, A. Caballero and S. S., "Molten Salts for Sensible Thermal Energy Storage: A Review and an Energy Performance Analysis.," *Energies,* vol. 14, p. 1197, 2021.
[17] S. Kuravi, J. Trahan, D.Y. Goswami, M.M. Rahman, E.K. Stefanakos, Thermal energy storage technologies and systems for concentrating solar power plants, Prog. Energy Combust. Sci. 39 (4) (2013) 285–319.
[18] U. Herrmann, B. Kelly, H. Price, Two-tank molten salt storage for parabolic trough solar power plants,", Energy 29 (5) (2004) 883–893.
[19] G. Angelini, A. Lucchini and a. G. Manzolini, "Comparison of Thermocline Molten Salt Storage Performances to Commercial Two-tank Configuration,," *Energy Procedia,,* vol. 49, p. 694–704, 2014.
[20] X. Py, Y. Azoumah, R. Olives, Concentrated solar power: Current technologies, major innovative issues and applicability to West African countries, Renew. Sustain. Energy Rev. 18 (2013) 306–315.
[21] L. Geissbühler and al., "An assessment of thermocline-control methods for packed-bed thermal-energy storage in CSP plants, part 2: assessment strategy and results," *Solar Energy,* vol. 178, p. 351–364, 2019.
[22] J. Hoffmann and al., ", Experimental and numerical investigation of a thermocline thermal energy storage tank,," *Appl. Therm. Eng.,* vol. 114, p. 896–904, 2017.
[23] S.G.Z. Yang, Molten-salt thermal energy storage in thermoclines under different environmental boundary conditions, Appl. Energy 87 (2010) 3322–3329.
[24] E. Oŕo and al., "Stratification analysis in packed bed thermal energy storage systems," *Appl. Energy,* vol. 109, p. 476–487, 2013.
[25] H. Yin and al., "Thermocline characteristics of molten-salt thermal energy storage in porous packed-bed tank," *Appl. Therm. Eng,* vol. 110, p. 855–863, 2017.
[26] T. Fasquelle and al., "Numerical simulation of a 50 MWe parabolic trough power plant integrating a thermocline storage tank," *Energy Convers. Manag.,* vol. 172, p. 9–20, 2018.
[27] T. Fasquelle and al., "A temperature threshold evaluation for thermocline energy storage in concentrated solar power plants,," *Appl. Energy,* vol. 212, p. 1153–1164, 2018.
[28] J.-F. Hoffmann and al., "A thermocline thermal energy storage system with filler materials for concentrated solar power plants: experimental data and numerical model sensitivity to different experimental tank scales," *Appl. Therm. Eng.,* vol. 100, p. 753–761, 2016.
[29] L. Nicolas and al., ", Flexibility and robustness of a high-temperature air/ceramic thermocline heat storage pilot,," *J.Energy Storage,* vol. 21, p. 393–404, 2019.
[30] R. Anderson and al., "Experimental results and modeling of energy storage and recovery in a packed bed of alumina particles,," *Appl. Energy,* vol. 119, p. 521–529, 2014.
[31] J. Pacheco, S. Showalter, W. Kolb, "Development of a molten-salt thermocline thermal storage system for parabolic trough plants," *J. Sol*, Energy Eng. 124 (2002) 153–159.
[32] P. Klein, T. H. Roos and a. T. J. Sheer, "Parametric analysis of a high temperature packed bed thermal storage design for a solar gas turbine,," *Solar Energy,* vol. 118, p. 59–73, 2015.
[33] E. Barbour, D. Mignard, Y. Ding, Y. Li, Adiabatic Compressed Air Energy Storage with packed bed thermal energy storage, Appl. Energy 155 (2015) 804–815.
[34] Ademe, "La chaleur fatale industrielle, Rapport D'étude," France (2015).
[35] I. Johnson, W. T. Choate and a. A. Davidson, "Waste Heat Recovery. Technology and Opportunities in U.S. Industry," *BCS, Inc., Laurel, MD (United States),* 2008.
[36] V. Novotny and al., "Review of Carnot Battery Technology Commercial Development," *Energies,* vol. 15, p. 647, 2022.
[37] J. Eggers and al., "Design and performance of a long duration electric thermal energy storage demonstration plant at megawatt-scale," *J.Energy Storage,* vol. 55, p. 105780, 2022.
[38] K. Knobloch and al., "Degradation of a rock bed thermal energy storage system,," *Appl. Therm. Eng.,* vol. 214, p. 118823, 2022.
[39] M. Al-Azawii and al., "Experimental study of layered termal energy storage in an air-alumina packed bed using axial pipe injection,," *Appl. Energy,* vol. 249, pp. 409-422, 2019.
[40] N. Hoivik, C. Greiner, J. Barragan, A. Iniesta, G. Skeie, P. Bergan, P. Blanco-Rodriguez, N. Calvet, Long-term performance results of concrete-based modular thermal energy storage system, J Energy Storage (2019) 24.
[41] N.Hoivik and al., "Long-term performance results of concrete-based modular thermal energy storage system," *J. Energy Storage,* vol. 24, p. 100735, 2019.
[42] J. Parham, P. Vrettos, N. Levinson, "Commercialisation of ultra-high temperature energy storage applications: The 1414 Degrees approach, Ultra-High Temp." Therm. Energy Storage Transf. Convers. (2021) 331–346.
[43] J. Briggs, " Antora Energy: Solid State Thermal Battery.," Arpa-E DAYS Annu. Meet., Advanced Research Projects Agency— Energy. 2021. , Available online: https://arpa-e.energy.gov/sites/default/files/2021-03/09Day1-JustinBriggs_AntoraEnergyreducedfilesize.pdf, 2021.

[44] A.R. Sane, P.-M. Nigay, D.P. Minh, C. Toussaint, A. Germeau, An investigation of the physical, thermal and mechanical properties of fired clay/SiC ceramics for thermal energy storage. l, J. Therm. Anal. Calorim. 140 (2020) 2087–2096.
[45] S. Aly, A. El-Sharkawy, Effect of storage medium on thermal properties of packed beds, Heat Recovery Syst. (1990) 509–517.
[46] A.R. Sane, Matériaux à base de phosphates pour le stockage thermique de l'énergie, IMT Mines Albi, France, Génie des procédés, 2017.
[47] M. Tawalbeh, H.A. Khan, A. Al-Othman, F. Almomani, S. Ajith, A comprehensive review on the recent advances in materials for thermal energy storage applications, International Journal of Thermofluids 18 (2023) 100326.
[48] A.R. Sane, D.P. Minh, N. Semlal, R. Boulif, C. Toussaint, A. Germeau, A. Nzihou, Clay/phosphate-based ceramic materials for thermal energy storage – Part I: Effect of synthetic phosphate content on microstructure, thermo-physical and thermo-mechanical properties, Open Ceramics 14 (2023) 100346.
[49] C. Xu, Z. Wang, Y. He, X. Li and a. F. Bai, "Sensitivity analysis of the numerical study on the thermal performance of a packed-bed molten salt thermocline thermal storage system," *Applied Energy,* vol. 92, p. 65–75, 2012.
[50] J.-F. Hoffmann, T. Fasquelle, V. Goetz and a. X. Py, "Experimental and numerical investigation of a thermocline thermal energy storage tank," *Applied Thermal Engineering,* vol. 114, p. 896–904, 2017.
[51] A. Gutierrez and e. al., "Advances in the valorization of waste and by-product materials as thermal energy storage (TES) materials," *Renewable and Sustainable Energy Reviews,* vol. 59, p. 763–783, 2016.
[52] A. Faik and al., "Thermal storage material from inertized wastes: Evolution of structural and radiative properties with temperature," *Solar Energy,* vol. 86, p. 139–146, 2012.
[53] I. Ortega, A. Faik, A. Gil and a. B. D. J. Rodríguez-Aseguinolaza, "Thermo-physical Properties of a Steel-making by-product to be used as Thermal Energy Storage Material in a Packed-bed System," *Energy Procedia,* vol. 69, p. 968–977, 2015.
[54] C. Xu, X. Li, Z. Wang, Y. He, F. Bai, Effects of solid particle properties on the thermal performance of a packed bed molten salt thermocline thermal storage system, Appl. Therm. Eng. 57 (2013) 69–80.
[55] G. Zanganeh, A. Pedretti, S. Zavattoni, M. Barbato, A. Steinfeld, Packed-bed thermal storage for concentrated solar power – Pilot-scale demonstration and industrial-scale design, Sol. Energy 86 (2012) 3084–3098.
[56] M. Cascetta, G. Cau, P. Puddu, F. Serra, Experimental investigation of a packed bed thermal energy storage system, J. Phys.: Conf. Ser 655 (1) (2015) 012018.
[57] H. Agalit, N. Zari, M. Maalmi, M. Maaroufi, "Numerical investigations of high temperature packed bed TES systems used in hybrid solar tower power plants", Sol. Energy 122 (2015) 603–616.
[58] M. Hänchen, S. Brückner, A. Steinfeld, "High-temperature thermal storage using a packed bed of rocks – Heat transfer analysis and experimental validation", Appl. Therm. Eng. 31 (2011) 1798–1806.
[59] T. Esence, A. Bruch, S. Molina, B. Stutz, J.-F. Fourmigué, A review on experience feedback and numerical modeling of packed-bed thermal energy storage systems, Sol. Energy 153 (2017) 628–654.